

Evaluation of acoustic Green's function in rectangular rooms with general surface impedance walls

Matteo Calafà*, Yuanxin Xia, Jonas Brunskog, Cheol-Ho Jeong

Acoustic Technology, Department of Electrical and Photonics Engineering,
Technical University of Denmark, 2800 Kongens Lyngby, Denmark

Abstract

Acoustic room modes and the Green's function mode expansion are well-known for rectangular rooms with perfectly reflecting walls. First-order approximations also exist for nearly rigid boundaries; however, current analytical methods fail to accommodate more general boundary conditions, e.g., when wall absorption is significant. In this work, we present a comprehensive analysis that extends previous studies by including additional first-order asymptotics that account for soft-wall boundaries. In addition, we introduce a semi-analytical, efficient, and reliable method for computing the Green's function in rectangular rooms, which is described and validated through numerical tests. With a sufficiently large truncation order, the resulting error becomes negligible, making the method suitable as a benchmark for numerical simulations. Additional aspects regarding the spectral basis orthogonality and completeness are also addressed, providing a general framework for the validity of the proposed approach.

1 Introduction

The room impulse response (RIR) plays a fundamental role in room acoustics, as it allows the derivation of several key acoustic parameters, including reverberation time and clarity [15], and it generally incorporates comprehensive information of the enclosed space [1, 32]. Moreover, under the assumption of a linear time-invariant (LTI) system, convolving the RIR with an arbitrary input signal directly yields the corresponding output sound field. The RIR is characterized by the Green's function, defined as the solution to the Helmholtz equation under a Dirac delta source [6, 16, 25]. Consequently, the computation of Green's functions is of paramount practical importance in many acoustic applications.

The numerical evaluation of the Green's function is however challenging due to the singular nature of the impulse source, which decreases the convergence rate of traditional numerical techniques such as the finite element method (FEM) [20, 2]. Alternatively, the boundary element method (BEM) requires the evaluation solely on the boundary of the domain avoiding to treat the singularity directly [28]. Some studies have instead employed singularity-removal strategies, in which appropriate representations of the solution capture the correct singular behavior and reduce the problem to determining only the regular part [8, 13]. Such singularity-removal techniques have also gained popularity in recent machine-learning-based (ML) approaches [14, 5].

An alternative technique for computing the Green's function in enclosures is based on spectral representations [30, 9], which rely on the expansion in terms of an orthogonal basis of room eigenfunctions (that in some contexts coincide with the resonance modes of the enclosure). However, this approach also has limitations: the eigenfunction set is infinite and typically unavailable in closed form. As a result, the eigenfunction expansion (EE) must be truncated and the single terms are usually computed numerically, leading to substantial computational cost, particularly when a large number of eigenfunctions is required.

In certain cases, explicit formulas for the eigenfunctions are available and can be exploited to construct the Green's function efficiently. For example, [27] derived the series representation for the

*matcal@dtu.dk

boundary value problem in the cylindrical domain. The most notable example, however, is the rectangular room with perfectly reflecting boundaries, for which closed-form modal solutions are well documented in classical acoustics literature [23, 16, 19]. Some works attempted to extend these results to more general boundaries. Specifically, [22] is among the earliest studies of first-order asymptotic expansions of eigenfunctions in rectangular rooms with surface impedance boundary conditions. More recently, [24] revisited underlying aspects of the derivation, including the orthogonality of the basis. Nevertheless, although these studies account for non-rigid boundaries, they remain limited to sufficiently hard walls, as they rely on asymptotics that assume the admittance to lie in a neighborhood of the origin. In this work, we broaden the analysis of rectangular rooms with absorbing boundaries by introducing additional first-order approximations that extend the range of validity to possibly any impedance value. Although closed-form solutions are generally unavailable, the proposed theory enables the development of an efficient, reliable, and accurate algorithm for evaluating the Green's function.

The manuscript is organized as follows: Section 2 introduces the physical models and the related mathematical problems under investigation. Section 3 is devoted to the derivation of the first-order eigenvalue approximations and mode solutions. Later, Section 4 describes the algorithm to compute the Green's function from the eigenfunctions and discusses the assumptions of basis orthogonality and completeness. Finally, some validation numerical tests are performed in Section 5 and conclusions are reported in Section 6.

2 Problem formulation

2.1 Mode and eigenvalue problems

We consider an open, connected and bounded domain $\Omega \subset \mathbb{R}^d$ in $d = 1, 2$ or 3 spatial dimensions. Under the time-harmonic condition, the acoustic field can be described by the Helmholtz equation with suitable boundary conditions (BCs). Specifically, imposing the normalized surface admittance $\beta : \partial\Omega \rightarrow \mathbb{C}$ (or, equivalently, the normalized surface impedance $\zeta = 1/\beta$) on the boundaries provides a general and accurate modeling framework for a wide range of physical configurations. The resulting boundary value problem (BVP) consists of finding the acoustic pressure $p : \Omega \rightarrow \mathbb{C}$ such that

$$\begin{cases} \nabla^2 p + k^2 p = s, & \text{in } \Omega, \\ \nabla p \cdot \mathbf{n} + ik\beta p = 0, & \text{on } \partial\Omega, \end{cases} \quad (1)$$

where $\nabla^2(\cdot)$ is the Laplacian operator, $s : \Omega \rightarrow \mathbb{C}$ is the source term and $k \in \mathbb{R}$ is the excitation wavenumber. For simplicity, dissipation in the medium is neglected, although this effect can be incorporated by allowing k to have a nonzero imaginary part. The particular case $\beta = 0$ corresponds to a Neumann BC, modeling perfectly rigid walls that reflect incident waves without dissipation or phase delay.

The Green's function $G_k(\cdot|\mathbf{x}_0) : \Omega \rightarrow \mathbb{C}$ is defined as the solution to Equation (1) under a Dirac impulse $s(\mathbf{x}) = -\delta(\mathbf{x} - \mathbf{x}_0)$ at $\mathbf{x}_0 \in \Omega$. Acoustic resonance modes can be introduced within the same framework. Namely, we state the *mode problem* as follows: find $\tilde{k} \in \mathbb{C}$ and $\phi \neq 0$ such that

$$\begin{cases} \nabla^2 \phi + \tilde{k}^2 \phi = 0, & \text{in } \Omega, \\ \nabla \phi \cdot \mathbf{n} + i\tilde{k}\beta \phi = 0, & \text{on } \partial\Omega. \end{cases} \quad (2)$$

The pair (\tilde{k}, ϕ) represents, respectively, the modal wavenumber and the associated modal pressure. Compared to the BVP, the source term vanishes and the wavenumber \tilde{k} becomes an additional unknown. Moreover, since the impedance may be frequency-dependent, β generally depends on the unknown \tilde{k} .

In this work, we further consider the following *eigenvalue problem*: given $k \in \mathbb{R}$, find $\hat{k} \in \mathbb{C}$ and $\varphi \neq 0$ such that

$$\begin{cases} \nabla^2 \varphi + \hat{k}^2 \varphi = 0, & \text{in } \Omega, \\ \nabla \varphi \cdot \mathbf{n} + ik\beta \varphi = 0, & \text{on } \partial\Omega. \end{cases} \quad (3)$$

Precisely, Equation (3) differs from Equation (2) as it introduces the different quantities k, \hat{k} . The two problems are nevertheless related, since any solution with $\hat{k} = k$ corresponds to a resonance

mode. In this setting, the solution pair (\hat{k}, φ) is instead identified by the eigenvalue $\lambda = -\hat{k}^2$ and the eigenfunction φ . Even if these terms depend on k , we decide to omit it for brevity of notation.

The motivation for introducing Equation (3) lies in the fact that eigenfunctions possess important mathematical properties that are generally not satisfied by the modal pressures. In previous literature, this distinction is often overlooked since, in the special case $\beta = 0$, the mode problem and the eigenvalue problem coincide, resulting in modes satisfying spectral properties. When impedance effects are included, however, the two formulations are no longer equivalent and $\tilde{k} \neq \hat{k}$.

In summary, we first introduced the Helmholtz BVP problem, for which the Green's function is a particular solution. We then formulated the modal problem and, subsequently, the associated eigenvalue problem. The solutions to the latter possess specific properties that are exploited in this work to construct the Green's function. We further note that k is real when interpreted as the physical wavenumber, whereas \tilde{k} and \hat{k} generally have nonzero imaginary parts, physically representing the loss introduced by $\beta \neq 0$. Finally, for clarity of exposition, quantities associated with the modal problem are denoted by a tilde $\tilde{\cdot}$, while those related to the eigenvalue problem are denoted by a hat $\hat{\cdot}$.

2.2 Problem formulation in rectangular rooms

We restrict the geometry to the rectangular room and assume β to be constant on each wall side. Under these assumptions, separation of space variables holds, and the problem in Equation (3) can be reformulated in 1D for each single axis. In particular, let us define $l \in \mathbb{R}^+$ the room size along the axis under consideration and $\beta_-, \beta_+ \in \mathbb{C}$ the normalized surface admittance on the left and right wall, respectively.

The general solution to the 1D homogeneous Helmholtz equation can be written as

$$\varphi(x) = \cos\left(\frac{\pi}{l}\hat{q}x + \hat{b}\right), \quad x \in \left[-\frac{l}{2}, \frac{l}{2}\right], \quad (4)$$

where $\hat{q}, \hat{b} \in \mathbb{C}$ need to be found by imposing the boundary conditions. In particular, $\hat{q} = \hat{k}l/\pi$ is proportional to \hat{k} and $\Lambda = \int_{\Omega} \varphi^2 d\mathbf{x}$ can be obtained explicitly as

$$\Lambda = \frac{l}{2} \left(1 + \frac{\sin(\pi\hat{q}) \cos(2\hat{b})}{\pi\hat{q}} \right). \quad (5)$$

Imposing Equation (4) into Equation (3), leads to the condition on \hat{q} :

$$((\pi\hat{q})^2 + \gamma_- \gamma_+) \tan(\pi\hat{q}) = i(\gamma_- + \gamma_+)(\pi\hat{q}), \quad (6)$$

where $\gamma_{\pm} := \beta_{\pm}kl$. \hat{b} can instead be found by solving

$$\pi\hat{q} \tan\left(\frac{\pi}{2}\hat{q} + \hat{b}\right) = i\gamma_+, \quad (7)$$

given \hat{q} . Equation (6) is equivalent to Equation (5.4) in [22] and Equation (8) in [24], corresponding to the generalization of the result from [23] for asymmetric walls. Specifically, it corresponds to a non-trivial transcendental equation in the single unknown \hat{q} , which admits no closed-form solution except in a few special cases. Among these, we highlight the choice of $\beta_- = \beta_+ = 0$, which reduces to the problem with perfectly rigid walls and whose solutions are $\hat{q} = \tilde{q} \in \mathbb{Z}$, as established by classical theory.

To summarize, Equation (6) represents the main problem to address, as all the other quantities can be directly inferred from \hat{q} , and separation of variables allows to extend the solution to 2D or 3D rectangular rooms.

3 Analysis of solutions

In this section, we investigate and derive approximations for the eigenvalues and modes of the rectangular room from the condition in Equation (6).

3.1 Analysis of eigenvalues

Some properties of Equation (6) can be readily deduced: $\hat{q} = 0$ is a solution and $+\hat{q}$ is a solution if and only if $-\hat{q}$ is. This is expected from the fact that $-\hat{k}^2$ is the eigenvalue of the problem. For such reason, we define $\mathcal{Q} \equiv \mathcal{Q}_- \cup \mathcal{Q}_+ \cup \{0\}$ the total set of solutions, by discerning the solution copies on the left and right side of the complex plane, respectively. In particular, we focus on only one side, say \mathcal{Q}_+ . Furthermore, let $\#_m \mathcal{Q}_+$ denote the number of solutions \hat{q} in \mathcal{Q}_+ such that $|\hat{q}| \leq m + \frac{1}{2}$.

We proceed by proving the following.

Theorem 1 (Number of solutions). *There exists $m_0 \in \mathbb{N}$ such that for any $m \geq m_0$:*

$$\#_m \mathcal{Q}_+ = \begin{cases} m, & \text{if } \gamma_- \gamma_+ = i(\gamma_- + \gamma_+), \\ m + 1, & \text{otherwise.} \end{cases}$$

Proof. Define $v_1(\hat{q}) = ((\pi\hat{q})^2 + \gamma_- \gamma_+) \sin(\pi\hat{q})$ and $v_2(\hat{q}) = -i(\gamma_- + \gamma_+) (\pi\hat{q}) \cos(\pi\hat{q})$, so that Equation (6) can be written as $v_1(\hat{q}) + v_2(\hat{q}) = 0$. Then, we have

$$\sup_{\hat{q} \in \partial B_m} \frac{|v_2(\hat{q})|}{|v_1(\hat{q})|} \leq \frac{|\gamma_- + \gamma_+| \pi (m + \frac{1}{2})}{\pi^2 (m + \frac{1}{2})^2 - |\gamma_- \gamma_+|} \sup_{\hat{q} \in \partial B_m} |\cot(\pi\hat{q})|,$$

where ∂B_m denotes the circumference of radius $m + \frac{1}{2}$. The first factor tends to zero as $m \rightarrow \infty$, while the second factor can be bounded by 2 for any m . Thus, by Rouché's theorem (see, e.g., Theorem 10.43 in [29]), the cardinality of \mathcal{Q} restricted to B_m is equal to that of the zeros of $v_1(\hat{q})$, i.e., $\mathbb{Z} \cap B_m$ and $\pm \sqrt{-\gamma_+ \gamma_-} / \pi$. Finally, if $\gamma_- \gamma_+ = i(\gamma_- + \gamma_+)$, the solution $\hat{q} = 0$ has triple multiplicity, single otherwise. By subtraction, the cardinality of \mathcal{Q}_+ can be determined. \square

In our setting, all solutions to Equation (3) must be found. Theorem 1 therefore provides a useful criterion for assessing whether the complete set of eigenvalues has been obtained. It is worth noting that, unlike the perfectly rigid case, the general problem admits an additional nontrivial eigenvalue.

3.2 First-order asymptotics of eigenvalues

Approximations of the solutions to Equation (6) can be found through the use of asymptotics of the $\tan(\cdot)$ function. In particular, we classify the approximate solutions according to different asymptotic regimes. In the following, we define $\gamma_- \parallel \gamma_+ := (\gamma_- \gamma_+) / (\gamma_- + \gamma_+)$, which corresponds to two resistors connected in parallel.

- Group 1 (hard walls):

Let

$$\begin{aligned} & - |\hat{q}|^2 \gg |\gamma_- \gamma_+|, \\ & - \hat{q} = n + \epsilon, \quad n \in \mathbb{N}_0, \quad |\epsilon| \ll 1. \end{aligned}$$

Then,

$$\begin{aligned} & - (\pi\hat{q}) \tan(\pi\hat{q}) \approx i(\gamma_- + \gamma_+), \\ & - \tan(\pi\hat{q}) \approx \pi\epsilon, \end{aligned}$$

$$\Rightarrow \hat{q} \approx \frac{1}{2} \left(n + \sqrt{n^2 + 4i \frac{\gamma_- + \gamma_+}{\pi^2}} \right), \quad n \in \mathbb{N}_0,$$

$$\text{if } \begin{cases} |\gamma_- \gamma_+| \ll n^2, \\ |\gamma_- + \gamma_+| \ll n, \end{cases} \quad \text{i.e., } |\gamma_-|, |\gamma_+| \ll n.$$

- Group 2 (soft walls):

Let

$$\begin{aligned} & - |\hat{q}|^2 \ll |\gamma_- \gamma_+|, \\ & - \hat{q} = n + \epsilon, \quad n \in \mathbb{N}_0, \quad |\epsilon| \ll 1. \end{aligned}$$

Then,

$$\begin{aligned} - (\gamma_- \parallel \gamma_+) \tan(\pi\hat{q}) &\approx i(\pi\hat{q}), \\ - \tan(\pi\hat{q}) &\approx \pi\epsilon, \end{aligned}$$

$$\Rightarrow \hat{q} \approx n \left(1 + \frac{i}{(\gamma_- \parallel \gamma_+) - i} \right), \quad n \in \mathbb{N}_0,$$

$$\text{if } \begin{cases} |\gamma_- \gamma_+| \gg n^2, \\ |(\gamma_- \parallel \gamma_+)| \gg n, \end{cases} \quad \text{i.e., } |\gamma_-|, |\gamma_+| \gg n.$$

- Group 3 (negative reactance):

$$\begin{aligned} \text{Let } \text{Im}(\hat{q}) \rightarrow +\infty &\Rightarrow \tan(\pi\hat{q}) \rightarrow i, \\ \Rightarrow ((\pi\hat{q})^2 + \gamma_- \gamma_+) &\approx (\gamma_- + \gamma_+)(\pi\hat{q}). \end{aligned}$$

$$\Rightarrow \hat{q} \approx \frac{\gamma_-}{\pi}, \frac{\gamma_+}{\pi},$$

$$\text{if } \text{Im}(\gamma_-), \text{Im}(\gamma_+) \gg 0, \text{ respectively.}$$

In group 1-3, we leveraged the $\tan(\cdot)$ expansion around the zeros and at the (imaginary) infinity. The case $\text{Im}(\hat{q}) \rightarrow -\infty$, similar to group 3, gives instead no admissible solutions. We include the asymptotics from the expansions around the poles:

- Group 1P (highly asymmetric walls):

$$\begin{aligned} |\hat{q}|^2 \gg |\gamma_- \gamma_+| &\Rightarrow (\pi\hat{q}) \tan(\pi\hat{q}) \approx i(\gamma_- + \gamma_+). \\ \hat{q} = n + \frac{1}{2} + \epsilon, n \in \mathbb{N}_0, |\epsilon| \ll 1 &\Rightarrow \tan(\pi\hat{q}) \approx -\frac{1}{\pi\epsilon}. \end{aligned}$$

$$\Rightarrow \hat{q} \approx \left(n + \frac{1}{2} \right) \left(1 + \frac{i}{\gamma_- + \gamma_+} \right), \quad n \in \mathbb{N}_0,$$

$$\text{if } \begin{cases} |\gamma_- \gamma_+| \ll n^2, \\ |\gamma_- + \gamma_+| \gg n, \end{cases} \quad \text{i.e., } |\gamma_{\pm}| \gg n, |\gamma_{\mp}| \ll n.$$

- Group 2P (not admissible):

$$\begin{aligned} |\hat{q}|^2 \ll |\gamma_- \gamma_+| &\Rightarrow (\gamma_- \parallel \gamma_+) \tan(\pi\hat{q}) \approx i(\pi\hat{q}). \\ \hat{q} = n + \frac{1}{2} + \epsilon, n \in \mathbb{N}_0, |\epsilon| \ll 1 &\Rightarrow \tan(\pi\hat{q}) \approx -\frac{1}{\pi\epsilon}. \end{aligned}$$

$$\Rightarrow \hat{q} \approx n + \frac{1}{2} + \frac{i(\gamma_- \parallel \gamma_+)}{\pi^2(n + \frac{1}{2})}, \quad n \in \mathbb{N},$$

$$\text{if } \begin{cases} |\gamma_- \gamma_+| \gg n^2, \\ |(\gamma_- \parallel \gamma_+)| \ll n, \end{cases} \quad \text{i.e., no allowed } \gamma_-, \gamma_+.$$

Asymptotics from group 1, 2, 3, 1P, 2P provide first-order approximations of the solutions to Equation (6), each one valid under the stated assumptions. Note, however, that in practice group 2P never applies, and group 1P is limited to the case in which the two walls differ significantly, e.g., one is very soft and the other is highly rigid. It is important to emphasize that previous literature [23, 24] only considered approximations from group 1, while omitting the other regimes. This has important consequences, as group 1 is valid only for sufficiently hard walls, whereas the characterization given above extends to possibly all types of impedance. In particular, group 1, 2 and 1P are complementary to each other, so that any combination of β_-, β_+ belongs to one of these groups or at their intersection. Group 3 is instead distinct as it provides one or two more solutions based on a fundamentally different assumption.

A practical criterion for selecting the correct group is given as follows: the cutoff from group 1 to 2, denoted by A_{1-2} , is obtained analytically as $A_{1-2} := \sqrt{|\gamma_- \gamma_+|}/\pi$. The transition from group 1 to 1P is instead identified by $A_{1-1P} := |\gamma_- + \gamma_+|/\pi$. There is no direct transition from group 2 to group 1P, since both the underlying assumptions of these groups differ. In addition, group 3 yields accurate approximations provided that the reactance is negative and not negligible with respect to

the resistance. Note that these criteria have been established theoretically and confirmed through numerical validation.

For perfectly symmetric walls where $\beta_- = \beta_+$, the two solutions in group 3 collapse to the same value. Therefore, we provide a correction to the previous formula. Let $\hat{q} = (\gamma + \epsilon)/\pi$ for $|\epsilon| \ll 1$, where $\epsilon = 0$ yields the original solution. Also note that $\tan(\pi\hat{q}) \approx (i - 2ie^{2i\pi\hat{q}})$ for $\text{Im}(z) \gg 0$, then Equation (6) gives

$$\epsilon^2 \approx 4\gamma^2 e^{2i(\gamma+\epsilon)} \Rightarrow \hat{q} \approx \frac{\gamma}{\pi}(1 \pm 2e^{i\gamma}), \quad (8)$$

where the first-order approximation of the Lambert W function is used. To summarize, Equation (8) provides a correction to the original group 3 estimate for discerning the two separate solutions when $\beta_- = \beta_+$.

3.3 Analysis of modes

Although our primary objective is to derive an eigenvalue representation of the Green's function, it is useful to briefly address to the mode problem for rectangular rooms. As introduced in Section 2, this corresponds to a particular case of the eigenvalue problem when $k = \hat{k}$. Imposing this condition in Equation (6) yields the following solution:

$$\tilde{q} = \frac{1}{\pi} \arctan \left(i \frac{\beta_- + \beta_+}{1 + \beta_- \beta_+} \right) + n, \quad n \in \mathbb{Z}. \quad (9)$$

Differently from the eigenvalue problem, the solution here is exact and can be obtained explicitly as long as the admittance is frequency-independent. Note that $\arctan(\cdot)$ has to be considered as the main branch of the associated multivalued function. Finally, observe that there is no solution symmetry along the real axis, in contrast to the eigenvalues examined earlier.

It is convenient to analyze the real and imaginary components of the modes separately. From Equation (9), we obtain

$$\text{Re}(\tilde{q}) = \frac{1}{2\pi} \arg(R_- R_+) + n, \quad n \in \mathbb{Z}, \quad (10)$$

$$\text{Im}(\tilde{q}) = -\frac{1}{2\pi} \ln |R_- R_+|, \quad (11)$$

where $R = (1 - \beta)/(1 + \beta)$ is the pressure reflection coefficient at the normal incidence angle. By definition, a room is in resonance when it is excited at the same frequency as one of its modes. As discussed in Section 2, the excitation frequency is constrained to be real-valued, which implies that resonance can occur only when $\text{Im}(\tilde{q}) = 0$. Consequently, $\text{Im}(\tilde{q})$ provides a meaningful measure of damping, and Equation (11) implies that damping prevents resonance in most cases except when $|R_- R_+| = 1$. Furthermore, the damping is maximized when either R_- or R_+ is equal to zero, corresponding as expected to perfectly absorbing boundaries.

The real part $\text{Re}(\tilde{q})$, on the other hand, can be interpreted as the excitation frequency closest to the modal frequency, i.e., the frequency at which the modal effect is most pronounced. Therefore, Equation (10) is particularly useful for identifying the locations of peaks in the transfer function. Notably, each value of $\text{Re}(\tilde{q})$ in Equation (10) is correctly restricted to the $[n, n + 1)$ interval.

4 Construction of Green's function

The representation of the Green's function as eigenfunction expansion (EE) lies on the assumption that eigenfunctions form an orthogonal and complete basis. In the case $\beta = 0$, this property is ensured by the spectral theorem for self-adjoint operators, yielding

$$G_k(\mathbf{x}|\mathbf{x}_0) = \sum_{n=1}^{\infty} \frac{\varphi_n(\mathbf{x})\varphi_n(\mathbf{x}_0)}{\Lambda_n(\hat{k}_n^2 - k^2)}, \quad (12)$$

where $\{(\hat{k}_n, \varphi_n)\}_{n=1}^{\infty}$ denotes all distinct eigenpairs of Equation (3) and $\Lambda_n := \int_{\Omega} \varphi_n^2 d\mathbf{x}$ is the normalization constant already introduced in Equation (5). In particular, Equation (12) leverages the fact that eigenfunctions are real-valued and orthogonal in $L^2(\Omega; \mathbb{R})$ for $\beta = 0$. In this section, we examine whether this result can be extended when the impedance is taken into account by analyzing the validity of the underlying assumptions.

4.1 Orthogonality of eigenfunctions

We recall that eigenfunctions are real-valued only for $\beta = 0$, therefore the analysis is carried out in $L^2(\Omega) \equiv L^2(\Omega; \mathbb{C})$ instead. Let $\langle \varphi_n, \varphi_m \rangle_{L^2(\Omega)} := \int_{\Omega} \varphi_n \overline{\varphi_m} d\mathbf{x}$ denote the standard Hermitian inner product, where $\overline{\varphi}$ is the complex conjugate of φ . It turns out that eigenfunctions are generally not Hermitian, i.e., $\langle \varphi_n, \varphi_m \rangle_{L^2(\Omega)} \neq 0$, however they satisfy

$$\langle \varphi_n, \overline{\varphi_m} \rangle_{L^2(\Omega)} = \int_{\Omega} \varphi_n \varphi_m d\mathbf{x} = 0, \quad \text{for } n \neq m. \quad (13)$$

This property was employed in [23] without explicitly proving it, whereas a demonstration was later given in the special case of rectangular domains by [24], and subsequently extended to general domains in [3]. Such result is in reality not specific to acoustic problems but holds in a much broader setting, as established below.

Theorem 2. *Let T be a function space and $\mathcal{B} : T \times T \rightarrow \mathbb{C}$ a bilinear form. Suppose $\mathcal{L} : T \rightarrow T$ is a \mathcal{B} -self-adjoint operator, i.e., $\mathcal{B}(\mathcal{L}u_1, u_2) = \mathcal{B}(u_1, \mathcal{L}u_2)$, $\forall u_1, u_2 \in T$. Then, any two eigenfunctions φ_1, φ_2 of \mathcal{L} corresponding to distinct eigenvalues are \mathcal{B} -orthogonal, i.e., $\mathcal{B}(\varphi_1, \varphi_2) = 0$.*

Proof. The proof is immediate and follows exactly the same passages adopted for the standard orthogonality. Namely, let $\lambda_n \neq \lambda_m$ be the eigenvalues associated to φ_n, φ_m , respectively. Then,

$$\begin{aligned} \lambda_n \mathcal{B}(\varphi_n, \varphi_m) &= \mathcal{B}(\mathcal{L}\varphi_n, \varphi_m) \\ &= \mathcal{B}(\varphi_n, \mathcal{L}\varphi_m) = \lambda_m \mathcal{B}(\varphi_n, \varphi_m), \end{aligned}$$

which implies that $\mathcal{B}(\varphi_n, \varphi_m) = 0$. □

Theorem 2 is stated in a broad setting and applies whenever self-adjointness is defined with respect to a bilinear form, rather than a sesquilinear inner product. It applies in our context by choosing $\mathcal{B}(\cdot, \cdot) = \langle \cdot, \cdot \rangle_{L^2(\Omega)}$. The resulting class of \mathcal{B} -self-adjoint operators is large, and in particular includes any operator of the form $\mathcal{L} = \sum_j \eta_j \mathcal{L}_j$, with $\eta_j \in \mathbb{C}$ and \mathcal{L}_j Hermitian. It follows that the Helmholtz problem in Equation (1) satisfies Equation (13) for any complex-valued parameters k and β , i.e., even when surface impedance or dissipation through the medium are taken into account.

An alternative way to interpret this result is to observe that, for such a class of operators, the eigenfunctions of \mathcal{L} and those of its adjoint \mathcal{L}^* are complex conjugates of each other, i.e., $\overline{\varphi_n} = \varphi_n^*$, $\forall n \in \mathbb{N}$. Consequently, Equation (13) follows automatically by the biorthogonality property [33].

In conclusion, Equation (12) requires no modification for $\beta \neq 0$ since it already accounts for the \mathcal{B} -orthogonality.

4.2 Completeness of the spectral basis

Completeness of the basis was long assumed to be true, and has only recently been examined in detail in [3]. The corresponding analysis is technical, and it requires the distinction between different definitions of completeness. We do not address these details here and instead refer the interested reader to the aforementioned work.

The central difficulty arises from the fact that the underlying operator is not self-adjoint, as discussed above, which obstructs the application of the spectral theorem. In general, a complete system may consist of both eigenfunctions and *generalized* eigenfunctions [18], which are defined iteratively as

$$\mathcal{L}\varphi_{n,j} = \lambda_n \varphi_{n,j} + \varphi_{n,j-1}, \quad j \in \mathbb{N},$$

where $\varphi_{n,0} = \varphi_n$ is the standard n -th eigenfunction. However, it can be seen that φ_n admits associated generalized eigenfunctions only if

$$\begin{aligned} \mathcal{B}(\varphi_n, \varphi_n) &= \mathcal{B}(\mathcal{L}\varphi_{n,1}, \varphi_n) - \mathcal{B}(\lambda_n \varphi_{n,1}, \varphi_n) \\ &= \mathcal{B}(\varphi_{n,1}, \mathcal{L}\varphi_n) - \mathcal{B}(\varphi_{n,1}, \lambda_n \varphi_n) = 0, \end{aligned}$$

where we have used the assumption of Theorem 2 on the second line. Notably, this condition is equivalent to $\Lambda_n = 0$, implying a zero denominator in Equation (12). We can then state the following.

Theorem 3. *The solutions φ to the problem in Equation (3) in the d -dimensional rectangular room with admittances $\beta_1, \beta_2, \dots, \beta_{2d}$ on each of the $2d$ walls form a complete basis for all admittance values except for a set $\Theta \subset \mathbb{C}^{2d}$ of zero Lebesgue measure.*

Proof. The set Θ in 1D is identified by the solutions of

$$\begin{cases} \sin(\pi\hat{q}) \cos(\hat{b}) = -\pi\hat{q}, \\ \frac{\pi}{2}\hat{q} \tan\left(\frac{\pi}{2}\hat{q} - \hat{b}\right) = \gamma_-, \\ \frac{\pi}{2}\hat{q} \tan\left(\frac{\pi}{2}\hat{q} + \hat{b}\right) = \gamma_+, \end{cases}$$

where the first equation follows by applying $\Lambda = \langle \varphi, \overline{\varphi} \rangle_{L^2(\Omega)} = 0$ from Equation (5), and the remaining two equations arise as intermediate steps in the derivation of (6) (see, indeed, Equation (7)).

Take any $\hat{q} \in \mathbb{C}$, then the associated \hat{b} is unique from the first equation except for multiples of π . It follows from the other two equations that the associated γ_-, γ_+ are unique. Furthermore, the map is holomorphic. Consequently, the set of admissible β_-, β_+ is contained in the image of a differentiable function from \mathbb{C} to \mathbb{C}^2 , which has zero measure [31]. The extension to $d > 1$ readily follows. \square

To summarize, we have verified that the orthogonality holds in a significantly larger setting and completeness is valid for almost every impedance parameter. Therefore, Equation (12) is guaranteed to hold as long as the problem parameters do not belong to the corresponding zero measure set.

4.3 Algorithm for calculation of Green's function

Finally, Algorithm 1 outlines a step-by-step procedure for evaluating the Green's function at a point \mathbf{x} due to an impulse source located at \mathbf{x}_0 , based on the results established in the preceding sections. First-order asymptotic approximations are used as effective initial choices for a Newton–Raphson scheme to fine-tune the solutions to Equation (6). Specifically, letting $v(\cdot) = v_1(\cdot) + v_2(\cdot)$ denote the residual of the equation and $v'(\cdot)$ its derivative with respect to \hat{q} , both quantities can be obtained in closed form, enabling an efficient and robust numerical implementation.

To accurately construct the Green's function, n_{\max} must at least be greater than $q := kl/\pi$, ensuring that the dominant terms in the series from Equation (12), for which the denominator is smallest, are included.

As already highlighted in Section 2, extending Algorithm 1 to 2D or 3D rooms is straightforward through separation of variables. In particular, one utilizes

$$\varphi_n(\mathbf{x}) = \prod_{j=1}^d \varphi_{n_j}(\mathbf{x}_j),$$

where φ_n denotes the n -th eigenfunction, with n being a multi-index $n = \{n_j\}_{j=1}^d \in \mathbb{N}^d$, and φ_{n_j} is the 1D eigenfunction from Algorithm 1. Furthermore, it can be verified that $\hat{k}_n^2 = \sum_{j=1}^d \hat{k}_{n_j}^2$. Thus, the total number of iterations is $(n_{\max} + 1)^d$. To conclude, Λ_n in Equation (12) can be obtained as the product of the 1D terms from Equation (5).

Algorithm 1 Evaluation of Green’s function (1D)

Require: $\beta_-, \beta_+ \in \mathbb{C}$.
Require: $l, k \in \mathbb{R}^+$
Require: $\mathbf{x}, \mathbf{x}_0 \in \Omega$.
Require: $n_{max}, n_{newton} \in \mathbb{N}$.
Require: $\alpha_{newton}, \varepsilon_{newton} \in \mathbb{R}^+$.
 $\mathcal{Q}_+ \leftarrow \emptyset$.
while $n = 0, \dots, n_{max}$ **do**
 while Group $\in \{1, 2, 3, 1P\}$ **do**
 if Assumption from Group (3.2) **then**
 Calculate \hat{q}_n from (3.2) and add to \mathcal{Q}_+ .
 end if
 end while
end while
while $n = 0, \dots, n_{newton}$ and $\varepsilon > \varepsilon_{newton}$ **do**
 $\mathcal{Q}_+ \leftarrow \mathcal{Q}_+ - \alpha_{newton} \frac{v(\mathcal{Q}_+)}{v'(\mathcal{Q}_+)}$.
 $\varepsilon \leftarrow \|v(\mathcal{Q}_+)\|_1$.
end while
if $\varepsilon > \varepsilon_{newton}$ **then**
 Raise warning.
end if
Remove copies from \mathcal{Q}_+ .
Remove $\hat{q} = 0$ from \mathcal{Q}_+ .
if Cardinality of $\mathcal{Q}_+ \neq n_{max} + 1$ (Theorem 1) **then**
 Raise error.
end if
 $G_k \leftarrow 0$.
while $n \in 0, \dots, n_{max}$ **do**
 $\hat{q}_n \leftarrow n$ -th element of \mathcal{Q}_+ .
 Get \hat{b}_n from Equation (7).
 Calculate φ_n at \mathbf{x}, \mathbf{x}_0 from Equation (4).
 Get Λ_n from Equation (5).
 Calculate $G_{k,n}$ from Equation (12).
 $G_k \leftarrow G_k + G_{k,n}$.
end while

5 Numerical tests

Some tests are here carried out to validate the results from the previous sections. For all the experiments, we consider the speed of sound in air $c = 343$ m/s. Codes have been implemented in Python 3.12 with minimal dependencies, in particular relying on NumPy 2.2.3 for vector computations [10]. The implementation of Algorithm 1 will be made available after the publication of this manuscript¹.

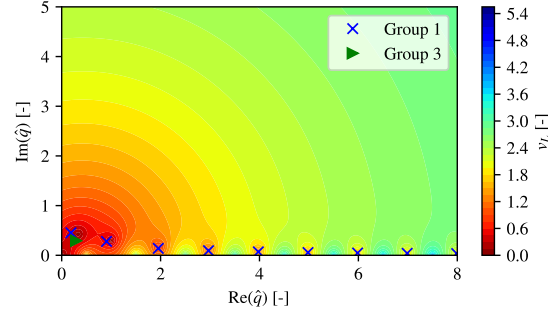
5.1 Approximation of eigenvalues

We begin by validating the first-order approximations derived in Section 3.2. Therefore, we consider the 1D problem with length $l = 1$ m, and $f = ck/(2\pi) = 5000$ Hz. Note that the choice of these parameters is largely arbitrary, since in Equation (6) they affect only $\gamma_{\pm} = \beta_{\pm}kl$, which also depends on β_{\pm} . Accordingly, we fix these parameters and evaluate the quality of the approximations by varying β_{\pm} instead.

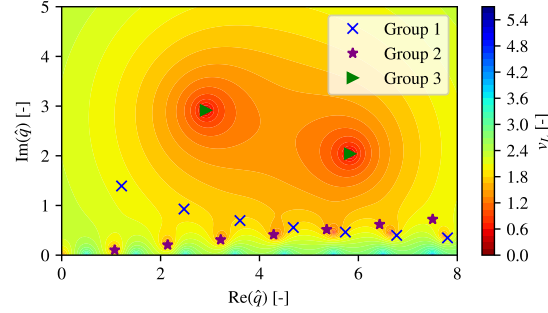
In order to assess the accuracy of the first-order asymptotics, we consider the quantity $v_L := \log_{10}(|v| + 1)$, where v was introduced earlier as the residual of Equation (6). The purpose of v_L is to numerically estimate the solutions \hat{q} by visualizing the contours on a more appropriate logarithmic scale. $v_L(\hat{q})$ is evaluated from $\text{Re}(\hat{q}) \in [0, 8]$, $\text{Im}(\hat{q}) \in [0, 5]$ on a uniform grid 500×800 . Three choices

¹<https://github.com/dtu-act/green-function-rect-rooms.git>

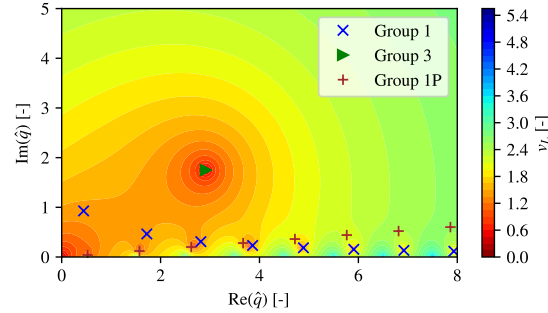
of admittance (β_-, β_+) are selected, and contour plots are reported in Figure 1. Exact solutions are identified by the red areas where $v_L = 0$, while approximations are displayed with different markers according to each group.



(A) $\beta_- = 0.01 + 0.01i$, $\beta_+ = 0.02$, $A_{1-2} \approx 0.49$.



(B) $\beta_- = 0.1 + 0.1i$, $\beta_+ = 0.2 + 0.07i$, $A_{1-2} \approx 5.05$.



(C) $\beta_- = 0.1 + 0.06i$, $\beta_+ = 0$, $A_{1-1P} \approx 3.40$.

Figure 1: Evaluation of eigenvalue first-order asymptotics from Section 3.2 for different admittance values. (A) Hard walls. (B) Soft walls. (C) Highly asymmetric walls. Admittance and cutoff transition values are provided.

Figure 1A displays a scenario characterizing hard walls. As expected, group 1 is sufficient to well represent all solutions. Group 3 is also added as the reactance on the left wall is negative and equal to the resistance. However, it can be noted that this is redundant, as it overrides group 1 to approximate the solution closer to the origin. We recall that $\hat{q} = 0$ is also present as the trivial solution. As expected, $A_{1-2}, A_{1-1P} < 1$, indicating that groups 2 and 1P shouldn't be included.

Softer walls are instead considered in Figure 1B, where $A_{1-2} \approx 5.05$ indicates that group 2 should be included for $n \lesssim 5$ in place of group 1, as confirmed by the graphics. Moreover, group 3 is included twice, as both reactances are not negligible and negative. Group 1P is instead omitted since the two admittances are of the same order.

A final scenario is shown in Figure 1C, where one wall is weakly soft with negative reactance, while

perfect reflection is applied on the opposite side. In this case, $A_{1-2} = 0$, indicating that group 2 should be disregarded. On the other hand, the strongly asymmetric configuration and $A_{1-1P} \approx 3.40$ suggest that group 1P should be included up to $n \approx 3$, as confirmed by the plot.

Figure 1 additionally validates Theorem 1, as $9=8+1$ solutions are visible in each of the three contour plots.

We emphasize again that Figure 1A corresponds to scenarios with hard walls examined in previous studies [23, 24], where group 1 was sufficient to approximate all eigenvalues. By contrast, increasing either the admittance order or the excitation frequency necessitates the inclusion of additional asymptotic groups, as illustrated in Figures 1B and 1C.

5.2 Calculation of Green's function

The eigenfunction expansion (EE) from Algorithm 1 is here employed to calculate the Green's function. A 2D rectangular room of size 1.0 m \times 1.4 m is tested with excitation frequency $f = 5000$ Hz, and the source point \mathbf{x}_0 is located at the coordinates [0.2 m, 0.2 m] with respect to the center of the room. Furthermore, we assign a different normalized surface impedance on each of the four walls: $\zeta_{-,x} = 10 - 3i$, $\zeta_{+,x} = 6$, $\zeta_{-,y} = 12 - 5i$, $\zeta_{+,y} = 4 - 4i$. The EE is employed with $n_{max} = 160 \gg q$, as recommended in Section 4.3. In addition, $n_{newton} = 100$, $\alpha_{newton} = 0.3$ and the tolerance to identify solution copies or the trivial $\hat{q} = 0$ is set to $\mathbf{tol} = 10^{-4}$.

Since no analytical solutions are available except the one proposed in this work, we benchmark our algorithm against a reference solution obtained from a conventional high-resolution numerical simulation. Specifically, a FEM solver is implemented in `FreeFEM 4.15` [11] using second-order Lagrange (P2) nodal elements. A uniform mesh with approximately 15 elements per wavelength (EPW) is employed, which is known to provide high accuracy [21]. This discretization results in $n_{DOF} = 380,557$ degrees of freedom. To treat the Dirac delta source, a singularity-removal strategy is adopted. Namely, the Green's function is decomposed as $G_k(\cdot | \mathbf{x}_0) = \Psi_k(\cdot | \mathbf{x}_0) + G_k^0(\cdot | \mathbf{x}_0)$, where

$$\Psi_k(\mathbf{x}|\mathbf{x}_0) = \begin{cases} \frac{i}{4} H_0^{(1)}(k|\mathbf{x} - \mathbf{x}_0|), & d = 2, \\ \frac{1}{4\pi|\mathbf{x} - \mathbf{x}_0|} e^{ik|\mathbf{x} - \mathbf{x}_0|}, & d = 3, \end{cases}$$

is the free-space fundamental solution of the Helmholtz equation, which captures the singularity at \mathbf{x}_0 , and $H_0^{(1)}(\cdot)$ denotes the Hankel function of the first kind. Therefore, the FEM problem is addressed to find only the singularity-free component G_k^0 .

The comparison of the two computed solutions is displayed in Figure 2, where they appear nearly identical, with only a minimal discrepancy at the singular source point. Interestingly, the effect of separation of variables in the eigenfunction expansion is visible with an increased error on the horizontal and vertical axes in correspondence of \mathbf{x}_0 .

We additionally aim to investigate the accuracy when varying the FEM mesh resolution and the truncation order in the EE. To account for this, we consider the $L^2(\Omega)$ relative error:

$$\mathcal{E}(p, p_{ref}) := \sqrt{\frac{\int_{\Omega} |p - p_{ref}|^2 d\mathbf{x}}{\int_{\Omega} |p_{ref}|^2 d\mathbf{x}}},$$

where the integrals are approximated by evaluating the terms on a large number (10^4) of uniformly sampled points in Ω . Furthermore, we consider a lower-fidelity FEM solution obtained with approximately 5 EPW, corresponding to $n_{DOF} = 43,717$. Errors are then computed between the evaluations from the EE for different values of n_{max} and the two FEM solutions, and are shown in Figure 3.

It is readily observed that the curve becomes steeper around $n_{max} = q \approx 40$, as expected from the discussion in Section 4.3. For $n_{max} \gtrsim q$, the error relative to the high-fidelity FEM solution continues to decrease gradually, in contrast to the other curve. This behavior may indicate that, for $n_{max} \gtrsim q$, the EE attains higher accuracy than the low-fidelity FEM solution.

A fair comparison of computational cost is challenging because of the fundamentally different methodologies and implementations (compiled versus interpreted language). Nevertheless, the total number of floating point operations in Algorithm 1 is approximately $10(n_{max} + 1)^d \approx 2 \times 10^4$, with $d = 2$ and $n_{max} \approx 40$. This is of the same order as n_{DOF} , but substantially smaller than the total number of nonzero matrix entries $n_{NZ} \approx 5 \times 10^5$ in the low-fidelity FEM. We therefore conclude that, in this respect, the EE approach is significantly more efficient than a traditional FEM implementation, both in terms of memory usage and computational time.

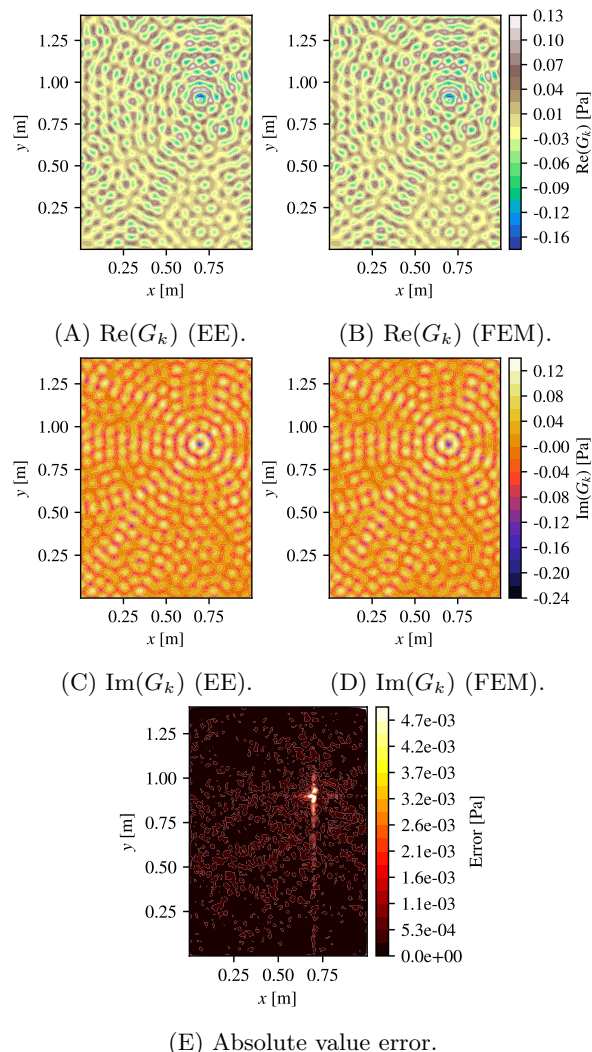


Figure 2: Comparison of the EE (Algorithm 1) and FEM simulation. The same color map is applied on each row. The two solutions appear considerably similar with a slightly larger error at the source singular location.

5.3 Analysis of modes

We dedicate a brief section to validate the results from Section 3.3 on resonance modes. Specifically, we consider a 1D domain of length $l = 1$ m, with a source at $\mathbf{x}_0 = 0.2$ m and a receiver at $\mathbf{x} = 0.8$ m. The EE is used on a frequency range $100 \text{ Hz} \leq f \leq 4000 \text{ Hz}$ with a resolution of 1 Hz. The sound pressure level (SPL) is then evaluated as $\text{SPL} = 20 \log_{10}(|G_k(\mathbf{x})|/p_0)$, where $G_k(\mathbf{x})$ is the computed Green's function from Algorithm 1 at the point \mathbf{x} and $p_0 = 2 \cdot 10^{-5}$ Pa is the reference sound pressure. The SPL is plotted in Figure 4 for three different choices of β_-, β_+ , along with $\text{Re}(\hat{q})$ from Equation (10).

As expected, the real parts of the room modes coincide with the peaks of the transfer function in all cases. In the figure, modes are also compared with those corresponding to perfectly rigid boundaries, revealing three distinct behaviors. In particular, Figure 4A exhibits a leftward frequency shift, whereas Figure 4B shows a rightward shift and a perfect overlap is visible in Figure 4C. These outcomes are expected and further validate Equation (10) since the condition $\beta_1 = \beta_2$ leads to $\arg(R_1 R_2) > 0$ if and only if $\text{Im}(\beta_1) = \text{Im}(\beta_2) < 0$ and the case $\beta_1 = \bar{\beta}_2$ yields $\arg(R_1 R_2) = 0$.

It should be emphasized that the values selected for β_-, β_+ are primarily intended for illustrative purposes and for validating the theory developed in Section 3.3. A detailed investigation of materials exhibiting such admittance values, particularly those associated with large and/or positive reactance, is beyond the scope of this work.

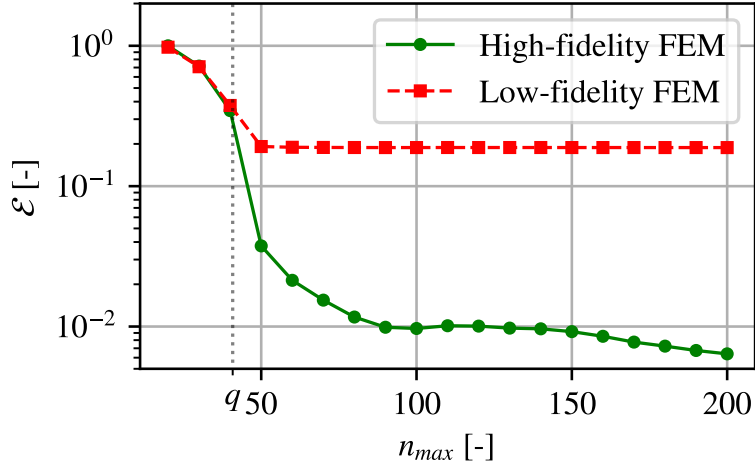


Figure 3: Convergence of the EE (Algorithm 1) as the truncation order increases. The error is shown relative to both the lower and high-fidelity FEM solutions. The value of q is marked as a vertical dotted line.

5.4 Comparison with measurements

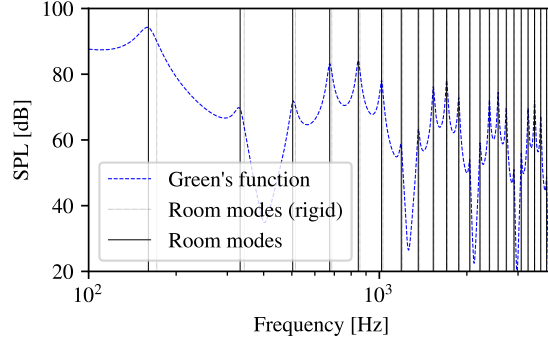
In this last experiment, we examine the method’s ability to predict the impulse response in a real room by comparing it with microphone measurements.

The room under investigation is an approximately rectangular space displayed in Figure 5. Measurements were carried out using a National Instruments 4431 data acquisition system, with signal amplification provided by a NAD 3020 amplifier. Acoustic responses were recorded using a Brüel & Kjær 4191 microphone, connected through type 2690 conditioning amplifiers and a NEXUS preamplifier. Excitation was provided by an exponential sine sweep sampled at 96 kHz, and the resulting transfer functions were computed via deconvolution with the inverse sweep followed by fast Fourier transform processing.

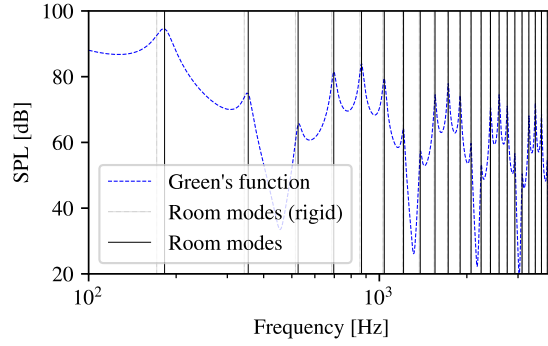
The room walls consist exclusively of concrete. The corresponding absorption coefficient was estimated using Eyring’s formula [7], yielding a value of $\alpha_{\text{concrete}} = 0.015$. The admittance, $\beta \approx 4 \times 10^{-3}$, was directly derived from α_{concrete} under the assumption of negligible reactance. The corresponding reflection coefficient R was obtained in the same manner. Algorithm 1 was then applied using the same parameter settings as in the previous test, over the frequency range $50 \text{ Hz} \leq f \leq 200 \text{ Hz}$ with a resolution of 0.1 Hz. Although values associated to higher frequencies can be computed in a reasonably short time, these are not reported since the increasing modal density makes the comparison more difficult to visualize. Room modes are additionally calculated from the formula in Equation (10). However, since $\text{Im}(R) = 0$, $\text{Re}(\tilde{q})$ trivially coincides with the classical result for perfectly rigid walls. Finally, the measured and computed SPL for the concrete room as well as the real part of the room modes are displayed in Figure 6A.

The two curves exhibit strong agreement on two fronts: first, the estimated absorption coefficient is validated by the comparable magnitude of the oscillations, indicating that the model captures the correct level of damping; second, the peak positions coincide with both the measured ones and those of the analytical room modes. This confirms the correctness of the theoretical derivation and supports the assumption of negligible reactance, showing that $\text{Im}(R)$ can be reasonably neglected in this test. Given the expected minimal numerical error of the EE, the remaining small discrepancies are more plausibly attributed to measurement uncertainties, inaccuracies in the impedance estimation, and imperfectly parallel walls due to construction tolerances.

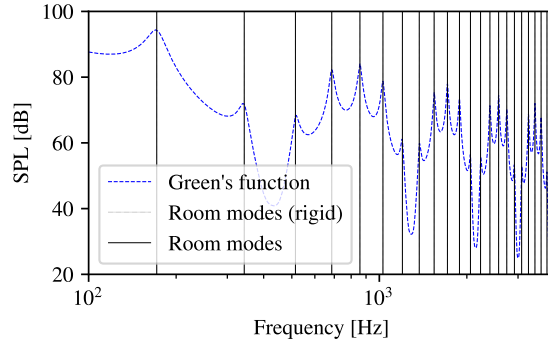
To further investigate asymmetric boundary conditions, an Ecophon Focus™ A panel is installed on the wall along the y -direction, opposite to the origin, as illustrated in Figure 5. The panel covers the entire wall surface, has a thickness of 20 mm, and a certified specific flow resistivity of $\Xi = 62,930 \text{ Pa s m}^{-2}$. The frequency-dependent impedance of the resulting two-layer wall is estimated using



(A) $\beta_- = \beta_+ = 0.1 + 0.1i$.



(B) $\beta_- = \beta_+ = 0.1 - 0.1i$.



(C) $\beta_- = 0.1 - 0.1i$, $\beta_+ = 0.1 + 0.1i$.

Figure 4: Comparison of Green's function with the analytical resonance modes from Equation (10).

the modified Allard & Champoux model [26]. Results for this second configuration are reported in Figure 6B, where good agreement is still observed.

To conclude, we aim to quantify the discrepancy between the measured and calculated Green's function. Owing to the presence of sharp modal peaks and dips, a point-wise error definition is inadequate. Instead, we adopt the Frequency Response Assurance Criterion (FRAC) [12, 17] as a similarity score from 0 (minimum similarity) to 1 (maximum similarity). Table 1 reports the pairwise FRAC for the four transfer functions obtained from the two configurations (denoted C and C+F). As expected, scores between signals associated with the same configuration are higher than those between different ones.

Regarding the use of asymptotic groups from Section 3.2, the configuration with exclusively concrete walls only employs group 1, as expected by the rigid materials and negligible reactance. In contrast, the addition of the absorber panel requires including group 1P, with $A_{1-1P} \approx 3$ at $f = 500$ Hz, as

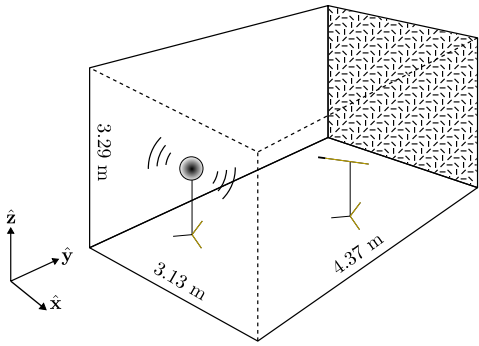
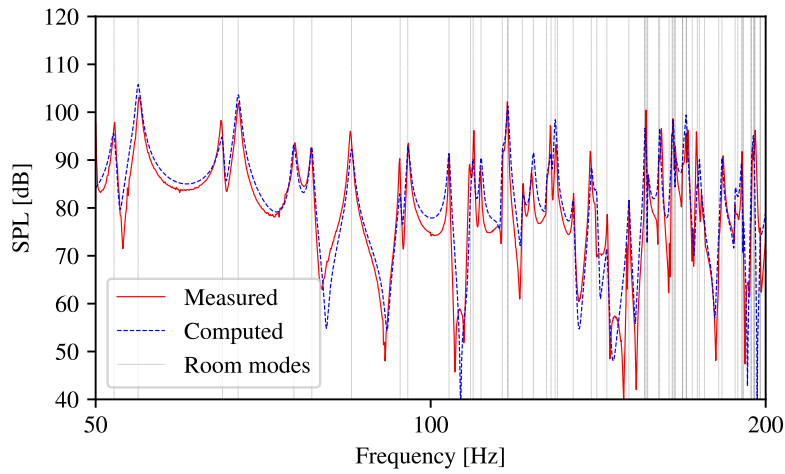
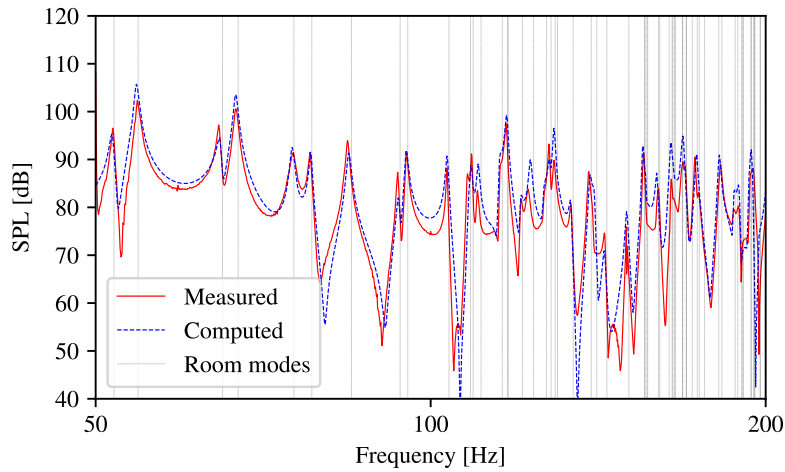


Figure 5: Sketch of the acoustic measurement room. The sound source is placed at coordinates [0.4 m, 0.396 m, 1.241 m] relative to the room corner, while the receiver is positioned at [0.567 m, 3.085 m, 1.033 m]. The absorbing panel is placed on the decorated wall face.



(A) Concrete walls.



(B) Concrete walls + Focus™ A panel.

Figure 6: Comparison of measured and computed SPL for the impulse response in the rectangular room. Analytical room modes from Equation (10) are also displayed as vertical lines.

	C(M)	C(EE)	C+F(M)	C+F(EE)
C(M)	–	0.66	0.41	0.42
C(EE)		–	0.47	0.61
C+F(M)			–	0.69
C+F(EE)				–

Table 1: Cross-evaluation of the FRAC score between the measured (M) and computed (EE) Green’s functions for the concrete room (C) and for the same room with the additional absorber (C+F).

expected by the diverging acoustic properties of the two wall faces.

6 Conclusions

This work investigates the use of eigenfunction expansions to construct the Green’s function in rectangular rooms with surface impedance boundary conditions. Since closed-form solutions cannot be obtained, first-order asymptotic approximations are developed. Notably, four distinct families of asymptotics are identified, each corresponding to a different impedance regime. This allows the calculation of the Green’s function for a wide range of impedance values, in contrast to previous studies that focused on a single family associated with sufficiently rigid walls. These first-order asymptotics provide effective initial choices for a Newton–Raphson scheme, allowing the accurate numerical computation of the eigenfunctions within a few iterations and with negligible error. Moreover, a criterion on the number of solutions is established, providing a reliable verification that all eigenfunctions have been obtained. The analytical framework also leads to closed-form expressions for resonance modes. The orthogonality and completeness of the resulting eigenfunction basis are subsequently examined: orthogonality is shown to hold in a very general setting, beyond the specific case of impedance boundary conditions for the Helmholtz problem, while completeness is proven for rectangular rooms. The extension of this result to more general settings remains instead an open problem (see, for instance, Open Problem 4.7 in [4]).

Numerical experiments first verify the proposed asymptotic expressions for the eigenfunctions and delineate their respective ranges of validity, confirming that all four asymptotic families may be required in practice. The Green’s function evaluation algorithm is then benchmarked against standard numerical solvers, demonstrating its superior accuracy and computational efficiency. Resonance modes are also computed and shown to coincide with peaks in the transfer function, with their locations shifting toward lower or higher frequencies depending on the impedance values. Finally, the computed Green’s function is compared with experimental measurements conducted in a 3D rectangular room, showing good agreement.

In conclusion, owing to its robustness and negligible error, the proposed algorithm represents a powerful alternative to conventional numerical solvers and can also serve as a reliable benchmark for numerical simulations. The present analysis further provides a foundation for future work, such as the development of second-order asymptotic approximations or the extension of the completeness theorem to more general geometries.

Acknowledgments

M.C. would like to thank Roland Badeau and Finn T. Agerkvist for valuable discussions.

Author declarations

Conflict of interest

The authors declare no conflict to disclose.

Data availability

Data will be made available on request.

References

- [1] F. Antonacci, J. Filos, M. R. Thomas, E. A. Habets, A. Sarti, P. A. Naylor, and S. Tubaro. Inference of room geometry from acoustic impulse responses. *IEEE Transactions on Audio, Speech, and Language Processing*, 20(10):2683–2695, 2012.
- [2] T. Apel, O. Benedix, D. Sirch, and B. Vexler. A priori mesh grading for an elliptic problem with Dirac right-hand side. *SIAM journal on numerical analysis*, 49(3):992–1005, 2011.
- [3] R. Badeau. On the spectral decomposition of the complex Robin Laplacian. *The Journal of the Acoustical Society of America*, 158(1):838–848, July 2025.
- [4] S. Bögli, J. B. Kennedy, and R. Lang. On the eigenvalues of the robin laplacian with a complex parameter. *Analysis and Mathematical Physics*, 12(1):39, 2022.
- [5] M. Calafà, H. M. Jensen, and T. Andriollo. Solving plane crack problems via enriched holomorphic neural networks. *Engineering Fracture Mechanics*, page 111133, 2025.
- [6] D. G. Duffy. *Green’s functions with applications*. Chapman and Hall/CRC, New York, New York, 2 edition, 2015.
- [7] C. F. Eyring. Reverberation time in “dead” rooms. *The Journal of the Acoustical Society of America*, 1(2A_Supplement):168–168, 1930.
- [8] I. G. Gjerde, K. Kumar, and J. M. Nordbotten. A singularity removal method for coupled 1D–3D flow models. *Computational Geosciences*, 24(2):443–457, 2020.
- [9] K. Habermann. Asymptotic error in the eigenfunction expansion for the Green’s function of a Sturm–Liouville problem. *Constructive Approximation*, pages 1–59, 2025.
- [10] C. R. Harris, K. J. Millman, S. J. van der Walt, R. Gommers, P. Virtanen, D. Cournapeau, E. Wieser, J. Taylor, S. Berg, N. J. Smith, R. Kern, M. Picus, S. Hoyer, M. H. van Kerkwijk, M. Brett, A. Haldane, J. F. del Río, M. Wiebe, P. Peterson, P. Gérard-Marchant, K. Sheppard, T. Reddy, W. Weckesser, H. Abbasi, C. Gohlke, and T. E. Oliphant. Array programming with NumPy. *Nature*, 585(7825):357–362, Sept. 2020.
- [11] F. Hecht. New development in freefem++. *Journal of Numerical Mathematics*, 20(3-4):251–266, 2012.
- [12] W. Heylen and S. Lammens. FRAC: a consistent way of comparing frequency response functions. In *Proceedings of the conference on identification in engineering systems*, pages 48–57, 1996.
- [13] M. B. Höltershinken, P. Lange, T. Erdbrügger, Y. Buschermöhle, F. Wallois, A. Buyx, S. Pursiainen, J. Vorwerk, C. Engwer, and C. H. Wolters. The local subtraction approach for EEG and MEG forward modeling. *SIAM Journal on Scientific Computing*, 47(1):B160–B189, 2025.
- [14] T. Hu, B. Jin, and Z. Zhou. Solving elliptic problems with singular sources using singularity splitting deep Ritz method. *SIAM Journal on Scientific Computing*, 45(4):A2043–A2074, 2023.
- [15] ISO 3382-1:2009: Acoustics – Measurement of room acoustic parameters. Standard, International Organization for Standardization, Geneva, CH, 2009.
- [16] F. Jacobsen and P. M. Juhl. *Fundamentals of general linear acoustics*. John Wiley & Sons, 2013.
- [17] C.-H. Jeong and J.-G. Ih. Effects of source and receiver locations in predicting room transfer functions by a phased beam tracing method. *The Journal of the Acoustical Society of America*, 131(5):3864–3875, 2012.

- [18] M. V. Keldysh. On the completeness of the eigenfunctions of some classes of non-selfadjoint linear operators. *Russian Mathematical Surveys*, 26(4):15–44, Aug. 1971.
- [19] H. Kuttruff. *Room acoustics*. CRC Press, Boca Raton, Florida, 2016.
- [20] H. Li, X. Wan, P. Yin, and L. Zhao. Regularity and finite element approximation for two-dimensional elliptic equations with line Dirac sources. *Journal of Computational and Applied Mathematics*, 393:113518, 2021.
- [21] S. Marburg. *Discretization Requirements: How many Elements per Wavelength are Necessary?*, pages 309–332. Springer Berlin Heidelberg, Berlin, Heidelberg, 2008.
- [22] P. M. Morse and R. H. Bolt. Sound waves in rooms. *Reviews of Modern Physics*, 16(3-4):324–324, July 1944.
- [23] P. M. Morse and K. U. Ingard. *Theoretical acoustics*. International series in pure and applied physics. McGraw-Hill, New York, New York, 1968.
- [24] M. Nolan and J. L. Davy. Two definitions of the inner product of modes and their use in calculating non-diffuse reverberant sound fields. *The Journal of the Acoustical Society of America*, 145(6):3330–3340, June 2019.
- [25] A. R. Okoyenta, H. Wu, X. Liu, and W. Jiang. A short survey on Green’s function for acoustic problems. *Journal of Theoretical and Computational Acoustics*, 28(02):1950025, 2020.
- [26] D. Oliva and V. Hongisto. Sound absorption of porous materials—accuracy of prediction methods. *Applied Acoustics*, 74(12):1473–1479, 2013.
- [27] C. Pérez-Arancibia and M. Durán. On the Green’s function for the Helmholtz operator in an impedance circular cylindrical waveguide. *Journal of computational and applied mathematics*, 235(1):244–262, 2010.
- [28] S. Preuss, C. Gurbuz, C. Jelich, S. K. Baydoun, and S. Marburg. Recent advances in acoustic boundary element methods. *Journal of Theoretical and Computational Acoustics*, 30(03):2240002, 2022.
- [29] W. Rudin. *Real and Complex Analysis*. McGraw-Hill International Editions Mathematics Series. McGraw-Hill, New York, New York, 3 edition, 1986.
- [30] Z. Sztranyovszky, W. Langbein, and E. Muljarov. Extending completeness of the eigenmodes of an open system beyond its boundary, for Green’s function and scattering-matrix calculations. *Physical Review Research*, 7(1):L012035, 2025.
- [31] T. Tao. *An introduction to measure theory*, volume 126 of *Graduate Studies in Mathematics*. American Mathematical Society, 2011.
- [32] S. Tervo, T. Korhonen, and T. Lokki. Estimation of reflections from impulse responses. *Building Acoustics*, 18(1-2):159–173, 2011.
- [33] A. Zhedanov. Biorthogonal rational functions and the generalized eigenvalue problem. *Journal of Approximation Theory*, 101(2):303–329, 1999.